UNIVERSITY OF ZIELONA GÓRA

CIVIL AND ENVIRONMENTAL ENGINEERING REPORTS

E-ISSN 2450-8594

CEER 2025; 35 (3): 0198-0220
DOI: 10.59440/ceer/207952
Original Research Article

ASSESSMENT OF CORRELATION BETWEEN INSAR COHERENCE AND MULTISPECTRAL INDICES FOR SOIL MOISTURE MONITORING

Aleksandra KACZMAREK[1], Roberto MONTI[2], Mirko REGUZZONI[2], Jan BLACHOWSKI[1]
[1] Wrocław University of Science and Technology, Department of Geodesy and Geoinformatics, Faculty of Geoengineering, Mining and Geology, Wrocław, Poland
[2] Politecnico di Milano, Department of Civil and Environmental Engineering, Milan, Italy

Abstract

Multispectral remote sensing has been widely used in surface water studies, including detection and monitoring of surface water dynamics, vegetation water content, peatland and wetland conditions, and soil moisture. Conversely, there is a limited number of research contributions on the potential applications of radar remote sensing and interferometric coherence in soil moisture monitoring. Addressing this gap, this study aims to investigate the relationship between radar data and selected spectral indices, with the purpose of joint monitoring of soil moisture changes. Furthermore, a quality index allowing for an a-priori assessment of the applicability of this combined methodology is proposed. The analysis is based on open access imagery acquired between 2019 and 2023 by ESA Copernicus Sentinel-1 and Sentinel-2 missions. The study focuses on two case study sites in Italy and Poland. The results indicate a significant correlation (0.70) between the two remote sensing datasets, highlighting the potential use of SAR coherence in soil moisture studies with both a stand-alone and a joint procedure.

Keywords: vegetation, DInSAR, coherence, remote sensing, spatial statistics

1. INTRODUCTION

Remote sensing has been widely used for the monitoring of various environmental components. Passive sensors usually provide data regarding the surface in the visible (VIS) and infrared (IR) range of the spectrum, while active sensors operate in radio and microwave frequencies. Depending on the wavelength, the signal can penetrate through the vegetation and the shallowest layers of the soil. The longer the wavelength, the deeper the penetration. However, this causes more noise (e.g., double bounce scattering, strongly enhanced volume scattering) [1, 2]. On the contrary to passive images, radar data

[1] Corresponding author: Aleksandra Kaczmarek, Department of Geodesy and Geoinformatics, Faculty of Geoengineering, Mining and Geology, Wrocław University of Science and Technology, 15 Na Grobli St., 50-421 Wrocław, aleksandra.kaczmarek@pwr.edu.pl, +48 70 320 68 27

are not affected by lighting conditions and meteorological factors such as snow and clouds. Thus, radar data could augment multispectral imagery in environmental studies.

Analysis of surface water dynamics using remote sensing has been subjected to a number or studies, including monitoring of drought [3], flooding [4], waterlogging [5-7], peat and wetlands [8, 9], soil moisture [10-13], and temporal changes in surface water area [14, 15]. Monitoring soil moisture based solely on remote sensing techniques poses challenges as acquired data refer only to the surface. Therefore, the contributions to soil moisture studies include in situ data of soil moisture [10-13, 16-18] for validation and verification. To enhance monitoring, data from various sensors and sources have been used [6]. In [10, 11, 13, 17, 18] data from multispectral and radar satellites were combined with in situ soil moisture measurements. Additionally, land cover classification was used in [6, 13].

Passive satellite missions such as Sentinel-2 or Landsat, provide open access to multispectral imagery that is used to calculate spectral indices aimed at highlighting selected elements of the environment. Water has moderate reflection in the visible (VIS, 400-700 nm) light region and strong absorption in short-wavelength infrared (SWIR, 1300-2500 nm). Plants with a higher water content tend to have lower reflectance in SWIR. Near infrared (NIR, 700-1300 nm) and SWIR have been used in studies of vegetation water content and soil moisture [19, 20]. The spectral signature of green vegetation shows great absorption in the VIS region and reflection in NIR [21]. Thus, analysis of vegetation condition can be used as an indirect method to monitor changes in surface water dynamics, as such changes affect plants causing water stress [22]. Information on soil moisture can be derived using the Soil Moisture Monitoring Index (SMMI) based on spectral reflectance in NIR and SWIR [23]. The SMMI was used to study mining subsidence, as due to mining activities, groundwater table sinks as a result of drainage from mining activities or is restored after end of mining, filling the subsidence basin [23].

Sentinel-1 backscatter, Normalized Difference Vegetation Index (NDVI), and Land Surface Temperature (LST) were used to investigate waterlogging in sugarcane yields [5]. In [24] the relationship between soil moisture and LST was pointed out, as the estimation of soil moisture requires a priori specification of LST, and vice versa. Spectral indices such as the NDVI, Normalized Difference Moisture Index (NDMI) or Normalized Difference Water Index (NDWI) were used in the assessment of waterlogging hazard [25] and in the development of vegetation distribution maps for the needs of flood mapping [4]. In studies [26, 27], a model was proposed for estimating soil moisture using a scatterplot of transformed SWIR reflectance and a vegetation index, such as NDVI. In [25] NDWI and the automated water extraction index (AWEI) were used to improve the analysis on dates when there was no radar data acquisition. Remote sensing data were analyzed together with topography derived from Digital Elevation Model (DEM) in [4, 25] or with Corine land cover in [13].

In addition to optical satellite imagery, Synthetic Aperture Radar (SAR) images are used for the analysis of soil moisture and surface water dynamics. It can be derived from the intensity of the backscatter [11, 13, 18, 28] or coherence, as changes in soil moisture influence the dielectric constant of the soil and, as a result, alter the refraction angle [29]. In [21] the differences between soil moisture estimation using coherence from C-band and L-band SAR imagery were discussed. The C-band data provide information on the top 5 cm level of the soil, while the L-band data provide deeper penetration and are less sensitive to temporal changes in vegetation. Therefore, they are less prone to temporal decorrelation [30]. However, C-band images have higher spatial resolution compared to L-band images. In [10], soil moisture information was retrieved using data from Sentinel-1 and Sentinel-2, and the quality of the estimates was assessed across various crop types. Noteworthy, the retrieval of soil moisture from SAR data depends on the incidence angle, as the estimation is more accurate at lower angles [31]. The greater the incidence angle, the higher the risk of estimation errors. Another factor that affects the analysis is polarization [18]. The VV polarization was proven to have better precision in

estimating soil moisture than the VH polarization. In [32], authors studied seasonality in the intensity and coherence of the SAR signal, and their link to seasonal changes in soil moisture and vegetation in peat. The intensity of the signal increases in the wet seasons, while coherence exhibits a negative correlation with changes in soil moisture. Sub-daily soil moisture variations using ground-based SAR sensors were studied in [33] in order to analyze the sources of decorrelation. The coherence varied depending on the soil moisture level, temperature, and daily vegetation cycle.

So far there are limited reports in the scientific literature on the potential application of SAR interferometric coherence in studies on soil moisture monitoring. Therefore, the purpose of this study is to investigate the relationship between selected spectral indices and SAR coherence. The findings of this analysis will allow to assess the potential use of radar data as complement to multispectral data, allowing for a comprehensive monitoring of soil moisture. Moreover, the joint use of data acquired by different sensors increases the number of observations in the time domain.

Additionally, this work will provide a quality index allowing for an a-priori assessment of the application of the joint methodology.

2. MATERIALS

The proposed workflow is tested in two different areas of interest (AOIs). The AOIs were selected in a way to test the methodology in areas of different characteristics, influence of industrial activity, as well as size and complexity, and thus check whether it can be successfully applied in various environments.

2.1. Areas of interest

The study is carried out in two specific areas selected because of their different environmental characteristics described below. The first AOI is an Underground Gas Storage (UGS) facility in Poland, while the second AOI represents an earth-filled dam on Arvo Lake in Italy.

The first AOI is a UGS facility located in Kosakowo, northern Poland at 54°36’22’’ N and 18°27’15’’ E (Fig. 1). The facility is used for storage of natural gas, which is kept in clusters of 5 caverns each, with a maximum storage volume of 295 million m³. They have been in operation since 2014. The storage caverns were constructed within the Permian Mechelinki rock salt deposit, which lies in the western part of the Peribaltic Syneclise [34]. The average thickness of the deposit is 170 m. The deposit lies at a depth of approximately 970 m below ground level. The geology of the region is mainly peat. The area above the Mechelinki salt deposit is located at an average altitude of 3 m above sea level, and in the basin of the Baltic Sea. Due to the given geological and topographic conditions, the area is susceptible to waterlogging.

The dam is located on the Arvo Lake in Calabria, southern Italy at 39°14’45’’ N and 16°32’45’’ E (Fig. 2). It is a critical infrastructure for the region as it ensures water supply throughout the year, for both agricultural and household use. The dam is located at an altitude of 1278 m above sea level. It is 27 m high and 280 m long. It is made of clay and compact soil. At the time of construction, it was the largest dam in Italy. The work began in 1926 with landscape transformation and earth mass displacement to create the dam and an underground tunnel for water adduction from the Ampollino lake. The tunnel has a length of slightly more than 6 km. The realization of the dam was possible due to the characteristics of the reservoir, which was less steep than other silane basins, and thus exerted less pressure on the dam itself. The Arvo Lake, which was created as a consequence of the barrage, has an area of 8 km^2 and capacity of 82 million m^3. Together with the Ampollino lake, they provide water to the Timpagrande hydroelectric power plant. The reservoir is supplied with water from 7 rivers: Arvo, Capalbo, Melillo, Cavaliere, Pugliese, Rovalicchio, and the underground tunnel from the lake Ampollino.

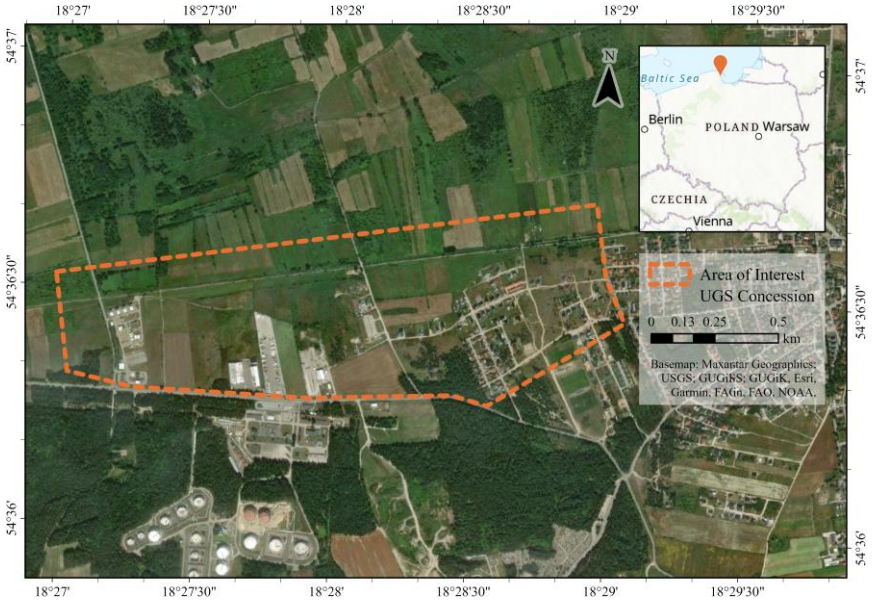

Fig. 1. Location of the underground gas storage facility in Kosakowo, Poland

Fig. 2. Location of the Nocelle Dam on Arvo Lake, Italy

2.2. Materials

In this study, two types of satellite remote sensing data were used, namely multispectral and radar imagery from the European Space Agency (ESA) Copernicus satellites.

Radar data were acquired by Sentinel-1. For the study, the images were downloaded from the Alaska Satellite Facility (ASF) Data Search Vertex (https://search.asf.alaska.edu/) that contains the complete Copernicus imagery catalogue. Level 1 (L1) Single Look Complex (SLC) Interferometric Wide-swath (IW) products were selected for the analysis. The IW SLC product is provided with one image per sub-swath and per polarization channel, for a total of three or six images. Each sub-swath image consists of a series of bursts, where each burst was processed as a separate SLC image. The individually focused complex burst images are included, in azimuth-time order, into a single sub-swath image, with black-fill demarcation in between. The images for all bursts in all sub-swaths of an IW SLC product are re-sampled to a common pixel spacing grid in range and azimuth [35]. For both study sites, imagery from ascending (ASC) and descending (DSC) tracks were selected (Table 1).

Table 1. Available radar images selected for analysis in both AOI

Area of Interest	**Nocelle Dam, Italy**		**Kosakowo UGS, Poland**			
Period	July 2019 – June 2023		March 2019 – November 2023			
Orbit	Ascending	Descending	Ascending		Descending	
Track	A146	D51	A102	A175	D22	D124
Number of images	187	184	217	189	213	205
Master epoch	04/06/2021	04/06/2021	13/06/2021	18/06/2021	14/06/2021	15/06/2021

The DEMs were downloaded for both AOIs. The DEM for the Italian AOI was downloaded from the regional Geoportal (http://geoportale.regione.calabria.it/opendata, accessed: 01/10/2024). A 5x5 m GRID model was selected for the study. It was created based on the results of the photogrammetric Calabria 2007-2008 campaign. The DEM for the Polish AOI was downloaded from the national Geoportal (https://mapy.geoportal.gov.pl/, accessed: 01/10/2024). Similarly to the Italian AOI, a 5x5 m GRID model was selected for the study, which is created based on the stereoscopic measurements made during the production of ortophotomosaics with pixel size of 25 cm.

3. METHODS

The processing was performed using Google Earth Engine [36] through the Python API, Python (version 3.12.2) and Matlab (version 2023b). The methodology adopted in our study consists of 4 main steps depicted in Fig. 3.

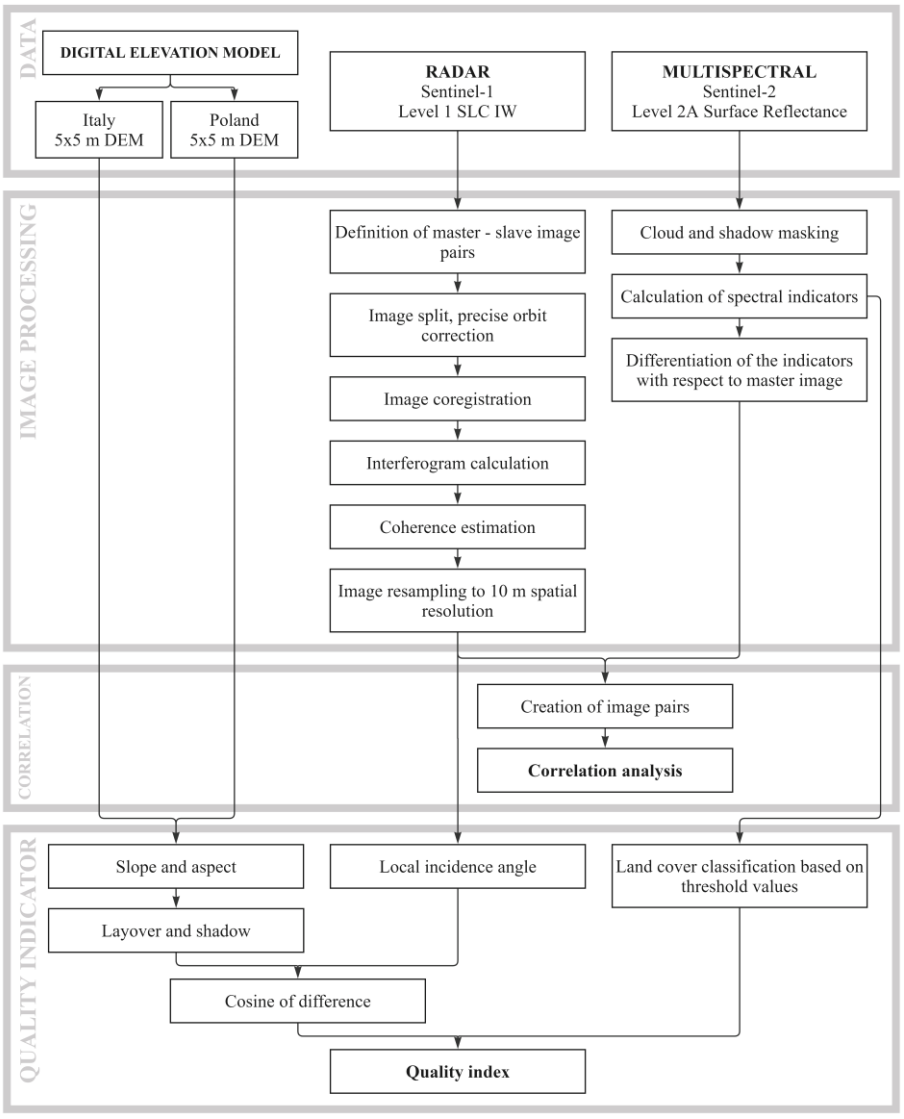

Fig. 3. Overview of the processing workflow for joint analysis of radar and optical data in soil moisture monitoring

3.1. Sentinel-1 processing

Radar imagery was processed using SNAP libraries through the PHASE software [37, 38]. To compute coherence (γ), which is a measure of similarity between two images, the master epoch for processing was determined. A date in the middle of the study period was selected for each of the tracks to reduce temporal decorrelation (Table 1) [39]. Then, the images were split by selecting the swath and burst(s) of interest. Precise orbit corrections were applied to the products. After that, image pairs of the master and slave dates were coregistered. For each pair, an interferogram was computed and coherence was estimated (Eq. 3.1) [40], which represents the correlation between two complex SAR images [41].

$$\gamma(r,c) = \frac{1}{N} \frac{\left|\sum_{r',c' \in W(r,c)} I_1(r',c') I_2^*(r',c')\right|}{\sqrt{\sum_{r',c' \in W(r,c)} |I_1(r',c')|^2 * \sum_{r',c' \in W(r,c)} |I_2(r',c')|^2}} \quad (3.1)$$

Where:
I_1, I_2 – images with *R* rows and *C* columns (they are the upper limits of the summations that are not reported in the formula for the sake of clarity),
I_2^* – complex conjugate of I_1,
$W(r,c)$ – sliding window centered in the pixel with row *r* and column *c*, where the coherence is evaluated,
r', c' – rows and columns of pixels inside the sliding window,
N – total number of pixels in the window.

The coherence was estimated with a sliding window of 2 pixels in azimuth (rows) and 10 pixels in range (columns). The final coherence value in each pixel is therefore an average of the coherence in all pixels inside the window. To convert the image from azimuth and range to projected coordinates [42], the so-called terrain correction was applied.

3.2. Sentinel-2 processing

The multispectral optical images of Sentinel-2 were accessed through the Google Earth Engine Data Catalog. The removal of clouds and cloud shadows was carried out using the s2cloudless algorithm [43].

The vegetation vigor and surface water dynamics, namely soil moisture changes and temporal occurrence of water in form of waterlogging, were analyzed using selected spectral indices derived from multispectral images. Each surface has specific reflectance properties that allow it to be identified based on the reflectance in visible and infrared parts of the spectra. NIR and SWIR spectra are of particular use, as they provide information about vigor and water content. SWIR is also suitable for the analysis of soil moisture. In this study, several commonly used indices to assess vegetation, soil moisture, and surface water dynamics, were computed (Table 2). Additionally, the Normalized Difference Built-up Index (NDBI) was selected to extract built-up features from the images.

Table 2. Spectral indices selected for the study. Band lengths used in the formulas: Blue 492 nm, Green 560 nm, Red 665 nm, NIR 842 nm, SWIR 1610 nm, SWIR2 2190 nm

	Name	Formula	Purpose	Source
Surface water	Automated Water Extraction Index (shadow)	$AWEI_{sh} = BLue + 2.5 * Green - 1.5 * (NIR - SWIR) - 0.25 * SWIR2$ (3.2)	Extraction of surface water bodies in urban areas. It eliminates shadows and dark features (urban shadow, mountains).	[44]
	Automated Water Extraction Index (no shadow)	$AWEI_{nsh} = 4 * (Green - SWIR) - (0.25 * NIR + 2.75 * SWIR2)$ (3.3)	Extraction of surface water bodies in urban areas. It is preferred in areas with no shadow present.	
Surface water	Normalized Difference Water Index	$NDWI = \frac{Green - NIR}{Green + NIR}$ (3.4)	Detection of surface water.	[45]

	Name	Formula		Purpose	Source
	Modified Normalized Difference Water Index	$MNDWI = \frac{Green - SWIR}{Green + SWIR}$	(3.5)	Detection of surface water. It is based on the NDWI, but the NIR was substituted with SWIR to remove the built-up areas noise.	[46]
Vegetation	Normalized Moisture Index	$NDMI = \frac{NIR - SWIR}{NIR + SWIR}$	(3.6)	Assessment of canopy water content. Flood and drought detection.	[47]
Vegetation	Normalized Difference Vegetation Index	$NDVI = \frac{NIR - Red}{NIR + Red}$	(3.7)	Assessment of vegetation vigor.	[48]
Soil moisture	Soil Moisture Monitoring Index	$SMMI = \frac{\sqrt{NIR - SWIR}}{\sqrt{2}}$	(3.8)	Assessment of soil moisture.	[23]
Built-up	Normalized Difference Built-Up Index	$NDBI = \frac{SWIR - NIR}{SWIR + NIR}$	(3.9)	Mapping built-up areas.	[49]

The SMMI index was normalized according to the following formula:

$$SMMI_{normalised} = \frac{SMMI - SMMI_{min}}{SMMI_{max} - SMMI_{min}} \quad (3.10)$$

where:
$SMMI_{min}$ – minimum value of *SMMI*,
$SMMI_{max}$– maximum value of *SMMI*.

3.3. Sentinel-1 and Sentinel-2 joint processing

Images were exported as geoTIFF rasters and then merged into a netCDF file, allowing further processing using Python.

To analyze multisensor data together, they must be uniform in time and space. The coherence images were upsampled using bilinear interpolation to match the spatial resolution of Sentinel-2 (10 m). Since coherence is a relative product, the spectral indices values were also differentiated with respect to the closest date to the epoch of the master image used in InSAR processing. To investigate the relationship between coherence and selected spectral indices, the images from both sensors were organized into pairs according to the acquisition date (allowable maximum difference of 1 day) (Table 3).

Table 3. Number of Sentinel-1 and Sentinel-2 image pairs

Area of Interest	**Nocelle Dam, Italy**		**Kosakowo UGS, Poland**			
Period	July 2019 – June 2023		March 2019 – November 2023			
Orbit	Ascending	Descending	Ascending		Descending	
Track	146	51	102	175	22	124
Number of image pairs	23	24	9	16	28	22

3.4.Statistical analysis

To investigate the correlation between SAR coherence and each of the selected multispectral indices, multiple scatter plots were created. Linear regression analysis was performed using the least squares method considering all the pixels within the AOI and replicating the procedure across all epochs and for all indices. The linear correlation coefficient was computed to numerically quantify the correlation level.

After that, all linear correlation coefficient values were put together in the same graph to show the correlation between SAR coherence and spectral indices as a function of time, identifying possible patterns. In addition to that, for each date and index, standard deviation of the residuals (Eq. 3.11) was computed to quantify the prediction error of the linear regression. The aim was to indicate the reliability of the slope estimate.

$$\sigma_{res} = \sqrt{\frac{1}{N-2}\sum_{i=1}^{N}(y_i - \hat{y_i})^2} \tag{3.11}$$

Where:
N – number of observations,
y_i – observed value of the indicator,
$\hat{y_i}$ - estimated value of the indicator from InSAR coherence via linear regression.

Moreover, all pixels were processed separately to investigate the temporal variation of the linear correlation between SAR coherence and selected multispectral indices. Therefore, for each pixel, the linear correlation coefficient was obtained. Finally, a threshold was applied to the obtained correlation maps to identify significant pixels, namely pixels exhibiting an absolute value of the linear correlation coefficient above the threshold of 0.35. The threshold value was selected based on the distribution of the obtained spatiotemporal correlation and its standard deviation.

3.5.Quality Index development

An index was proposed to a priori assess the likelihood of the correlation between SAR coherence and spectral indices. This quality index (Q_{index}) is based on two types of remotely sensed data. The first group relies on radar contributions, such as the local incidence angle, the layover, and the shadow computed from the slope and the aspect derived from DEM. As the quality of soil moisture estimation depends on the incidence angle and the sensing geometry, the contribution of SAR to the overall quality index was considered significant. The second part of the formula includes the basic classification of land cover based on spectral indices. Certain threshold values were selected to distinguish vegetation, surface water, and built-up areas. The threshold values used in the study are given in Table 4. Then, weights were assigned to each of the described elements. Areas with dense vegetation were assigned lower weights

because such areas provide poor interferometric coherence and, thus, low quality. The final index was created using the conditions stated in 3.12, 3.13 and formulae 3.14-17.

$$Lo = \begin{cases} -1 & if \quad \cos(A-\theta) \geq \tan(S) \\ 1 & if \quad \cos(A-\theta) < \tan(S) \end{cases} \tag{3.12}$$

$$Sh = \begin{cases} -1 & if \quad S \geq \text{LIA} \\ 1 & if \quad S < LIA \end{cases} \tag{3.13}$$

$$Cd = \cos(LIA - A) \tag{3.14}$$

Where:
Lo – layover,
A – aspect,
θ – azimuth,
S – slope,
Sh – shadow,
LIA – local incidence angle,
Cd – cosine of angle difference.

The quality index for radar data, which ranges from -1 to 1, is:

$$Q_{index,S-1} = Cd * w_{Cd} - L * w_{Lo} - Sh * w_{Sh} \tag{3.15}$$

The quality index for optical contributions, which ranges from -1 to 1, is:

$$Q_{index,S-2} = Q_{NDWI} * w_{NDWI} + Q_{NDVI} * w_{NDVI} + Q_{NDMI} * w_{NDMI} + Q_{NDBI} * w_{NDBI} \tag{3.16}$$

The final quality index:

$$Q_{index} = Q_{index,S-1} * w_{S-1} + Q_{index,S-2} * w_{S-2} \tag{3.17}$$

The Q_{Index} was rescaled so the values range from 0 to 1, to make the interpretation easier. Weights in Table 4 were empirically calibrated based on a training set and iteratively modified to obtain optimal results with respect to the expected outcome.

Table 4. Parameters used in the quality index with assigned weights. Nested levels refer to the constitutive contributions used to create the index, e.g., for Sentinel-2 (Level 1) four indices (Level 2) are considered and each of them is classified based on threshold values (Level 3). Each parameter has an assigned weight

Parameters			**Weights**		
Level 1	Level 2	Level 3	Level 3	Level 2	Level 1
Sentinel-1	Cd	-	-	0.70	0.60
	Lo	-	-	0.15	
	Sh	-	-	0.15	
Sentinel-2	NDWI	< -0.3	0.15	0.30	0.40
		-0.3 – 0.0	0.55		
		0.0 – 0.2	0.15		
		> 0.2	0.15		

Parameters			Weights		
Level 1	Level 2	Level 3	Level 3	Level 2	Level 1
	NDVI	< 0.2	0.70	0.30	
		0.2 – 0.5	0.25		
		> 0.5	0.05		
	NDBI	< 0.0	0.10	0.20	
		≥ 0.0	0.90		
	NDMI	< -0.2	0.70	0.20	
		-0.2 – 0.0	0.20		
		0.0 – 0.2	0.05		
		> 0.2	0.05		

3.6. Validation of the quality index

The validation of a newly developed index is crucial to ensure its effectiveness and alignment with the intended purpose. In the context of this study, this process was performed according to the following steps. Pixels were divided based on their Q_{Index} value, distinguishing between high quality (above 0.70) and low quality (below 0.50). Then, linear regression was performed, considering multispectral-derived SMMI as response and SAR coherence as predictor. The coefficients of the single-variable linear regression were estimated using least squares compensation (e.g., mean value and angular coefficient for the SAR coherence). On both estimated parameters a t-test to estimate their significance was done. If the empirical t-value was smaller than the t-limit value, the parameter was deemed as non-significant and therefore removed; another iteration of the least squares solution would therefore be required on the reduced model. Additionally, the normalized root mean square error (NRMSE) was computed to quantify the error level.

4. RESULTS

4.1. Time series of correlation between SAR coherence and MS indices

The MS indices were computed for all images available within the analysis period, but the correlation with SAR coherence was investigated only for image pairs (Table 3). The correlation between SAR coherence estimated from images of both ascending and descending tracks was checked. Additionally, two variants of signal polarization, namely vertical-vertical (VV) and vertical-horizontal (VH), were considered. As a result, the ASC track 146 in VV polarization was selected for the Nocelle Dam, while for the Kosakowo UGS the DSC 22 in VV polarization, provided the optimal output. The temporal profile of average correlation values and the standard deviations are shown in Fig. 4 and Fig. 5, for the Nocelle Dam and Kosakowo UGS, respectively. The automated water extraction indexes and the MNDWI were rejected due to a highly dispersed distribution of values in the study areas. Their time series differed significantly from the remaining indices.

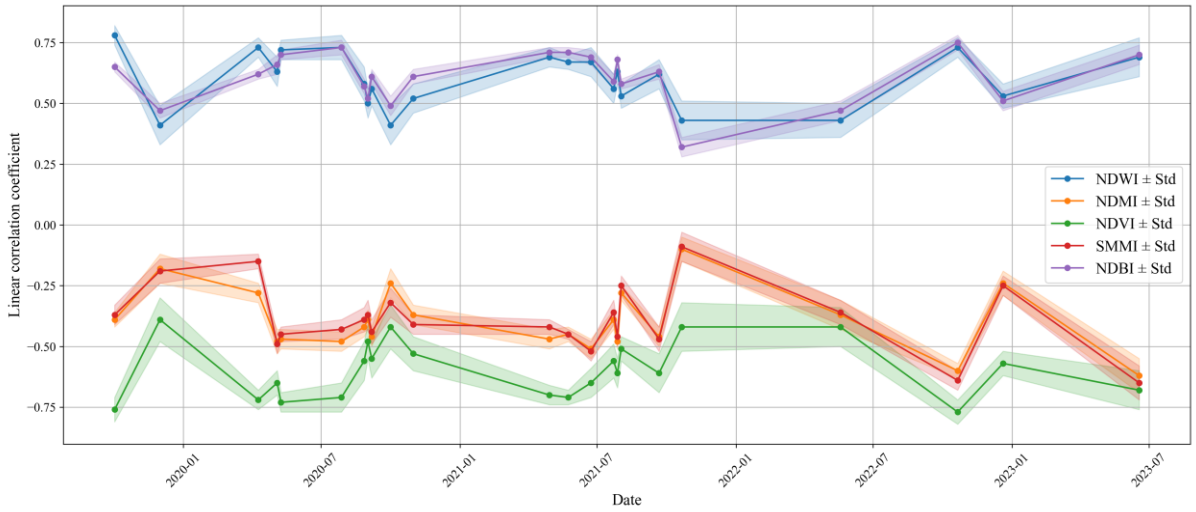

Fig. 4. Average correlation between MS indices and SAR coherence from ASC track 146 with standard deviations in the Nocelle Dam area

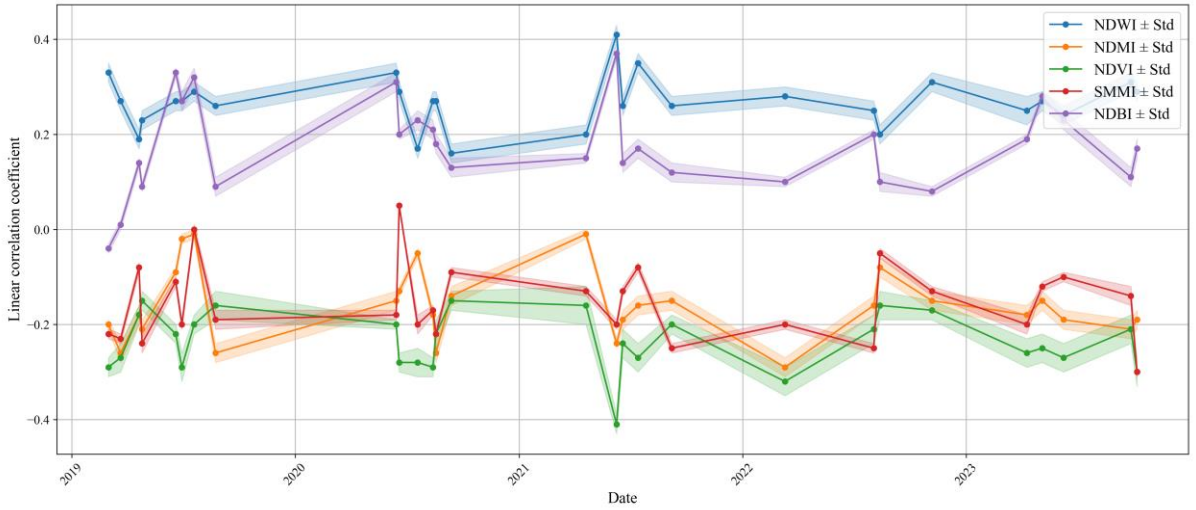

Fig. 5. Average correlation between MS indices and SAR coherence from DSC track 22 with standard deviations in the Kosakowo UGS area

A similar temporal pattern is observed in both AOIs but at different magnitudes. The dam within the Italian AOI is a smaller structure compared to the second AOI. Furthermore, the land cover is more homogeneous in that area, since the downstream face of the dam is covered with grass and the other side is made of stones and concrete. In general, a strong relationship between the selected indices and SAR image coherence can be observed at the site. The study region in Poland is more diverse, since it includes roads, crops, forests, and built infrastructure, which is reflected in the average values of the multispectral indices and generally a lower correlation with coherence. Fig 6. shows the linear correlation for all considered multispectral indices, across both AOIs. The estimated linear regression line passes very close to the scatter points, further confirming the similarity pattern observed for the Italian and Polish sites.

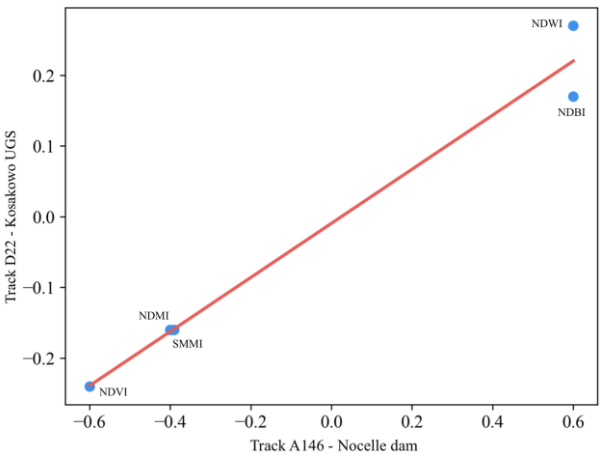

Fig. 6. Visualization of the linear correlation for all indices across the two AOIs

Two groups of multispectral indices are identified. The first group exhibits a positive correlation with the coherence. The NDWI is used to delineate surface water bodies, while the NDBI is used to extract built-up features. The built-up infrastructure has positive NDBI values [49], has high stable backscattering, and high stability over time [50]. On the other hand, the indices used in vegetation and soil moisture studies show a negative relationship with coherence. A strong correlation is observed for NDVI, as the correlation drops to -0.75 in the dam and -0.40 in the UGS site. Little or no consistency can be found in densely vegetated regions. Inverse temporal patterns can be observed between the two groups. The temporal interval between consecutive image pairs is not equal; thus, winter periods are smoothed because of the lack of clear Sentinel-2 images. The correlation was also plotted separately for all indices and dates (Fig. 7, 8). A linear trend was fitted to each of the images. Both NDWI and NDBI have positive correlation with values during winter lower (image acquired on 01/12/2019) than in Spring and Autumn. Indices used for assessment of vegetation, vegetation water content, and soil moisture have a negative impact on the interferometric coherence, which is confirmed by negative correlation. For the Kosakowo UGS site, the correlation is lower, and the scatterplots are more random. No significant pattern within a single image can be clearly identified.

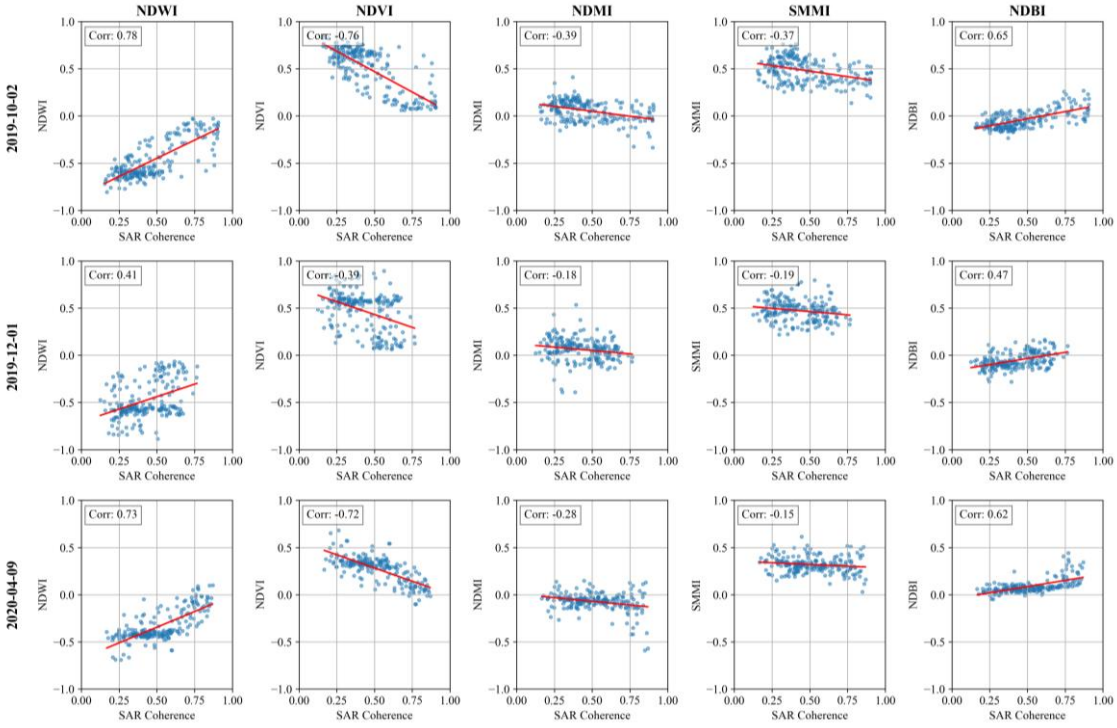

Fig. 7. Scatterplots of SAR coherence (ASC track 146) and MS indices in Nocelle dam on 3 consecutive dates

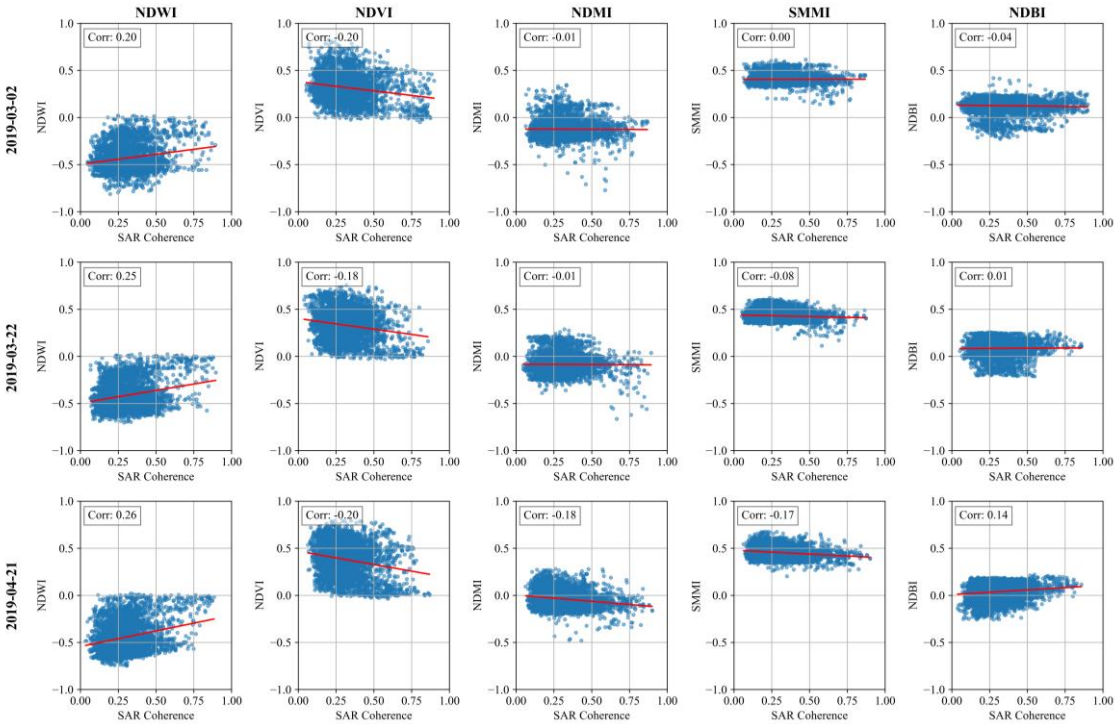

Fig. 8. Scatterplots of SAR coherence (DSC track 22) and MS indices in Kosakowo UGS on 3 consecutive dates

The pixel-wise correlation coefficient values for the Nocelle dam are shown in Fig. 9. According to previous results, two types of correlation are identified based on the multispectral index used. The pixels were classified into areas of positive, negative, or no correlation. In all investigated cases, clusters of pixels with significant correlation were identified in the central part of the dam.

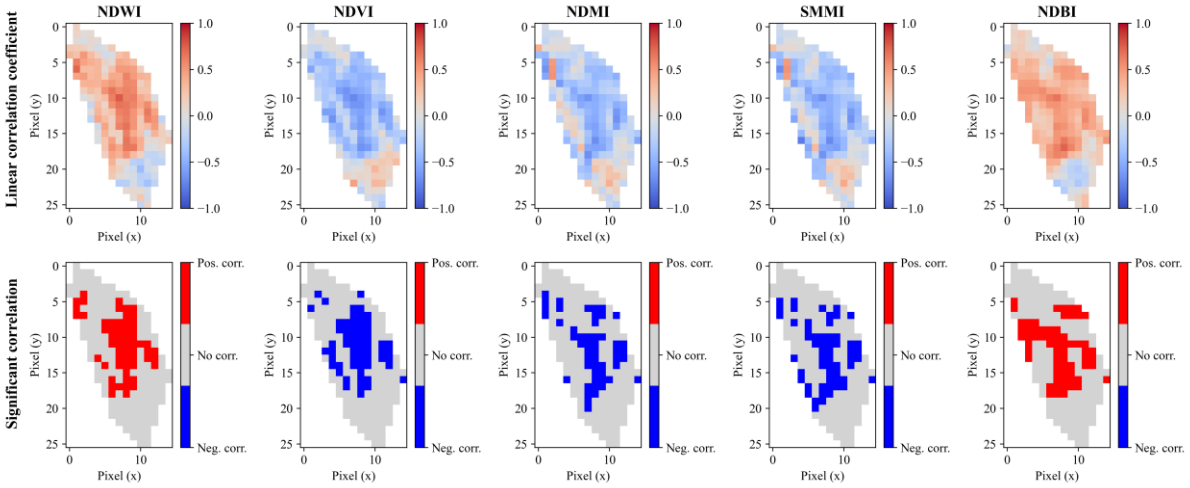

Fig. 9. Correlation coefficients between multispectral indices observed in the Nocelle Dam AOI

The pixel-wise linear correlation coefficient shown in the first row of images of Fig. 9 required estimation of both slope and intercept of the regression line. This allows us to create maps showing the value of these two quantities for each (significant) pixel, as well as the least squares interpolation result. Fig 10. provides, as an example, the case of the SMMI.

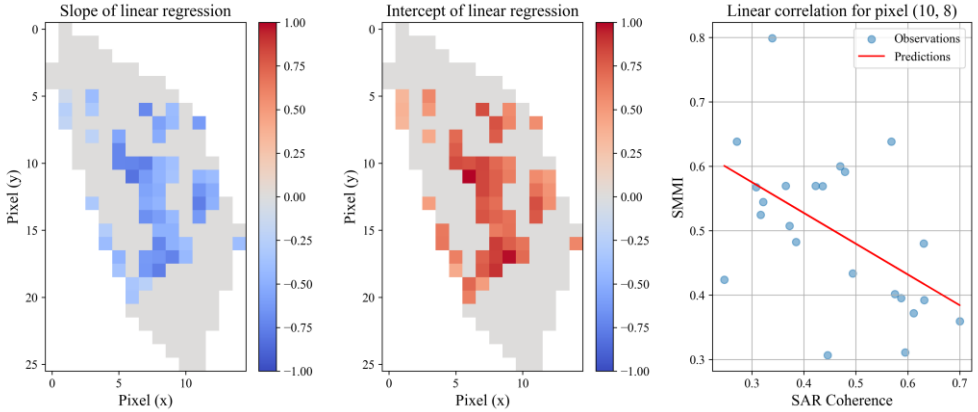

Fig. 10. Slope and intercept of linear regression between SAR coherence and SMMI, together with a regression line example for a randomly selected pixel

4.2. Development of the quality index

Based on the observed characteristics of both study areas, further analysis was limited to the Nocelle Dam as it exhibited higher linear correlation between the investigated factors.

The quality index was built using radar and optical data. Radar images have different viewing geometry depending on the interaction between the SAR line of sight and the surface orientation, thus having a crucial impact on the quality of radar interferometry processing. A cosine of difference between the local incidence angle and aspect highlights areas with optimal sensing potential. The dam is divided by its crown into two clusters (Fig. 11). The grass-covered downstream face side has favorable conditions for InSAR monitoring, while the water-facing side is limited by shadow.

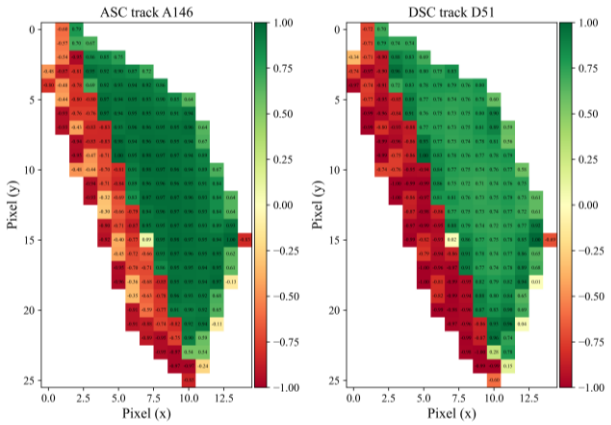

Fig. 11. Cosine of the difference between the local incidence angle and the aspect for the ascending (left) and descending (right) tracks

To define the classes using multispectral indices, the reference image was selected for clustering. All pixels within the AOI were divided into several groups according to their values. The classification was performed manually to minimize the complexity of the workflow. The NDBI image was divided into two classes. Positive values correspond to built-up features, and negative values represent non-built areas [49]. Due to the stability of the backscatter of urban areas over time, built-up areas are desired in InSAR processing. For the sake of brevity, classification based on only one index is presented in the study. The NDVI was used to extract areas of no vegetation, moderate and dense vegetation (Fig. 12). The concrete wall of the dam was correctly identified as a non-vegetated area, while the grass-covered wall had NDVI values exceeding 0.5.

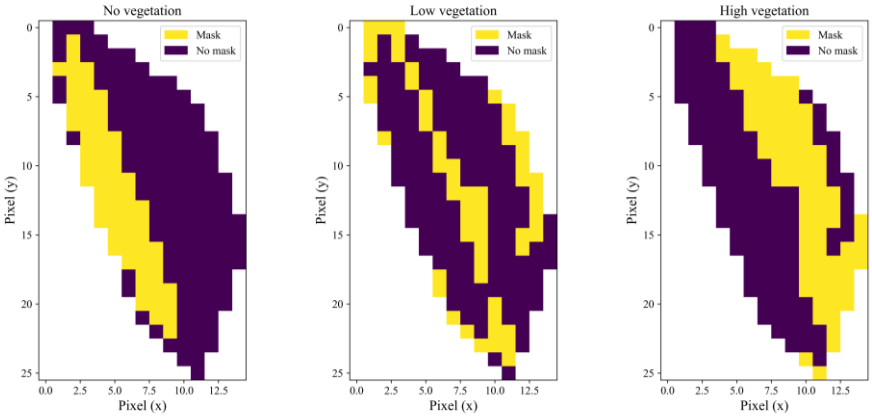

Fig. 12. Pixel classification based on NDVI values. The area is divided into no vegetation (left), low vegetation (center), and high vegetation (right)

The NDMI was split into 4 classes. Bare soil and low canopy values are represented by values lower than -0.2. The next group represents areas with low canopy under water stress. Values between 0 and 0.2 correspond to a higher canopy under water stress. Positive values represent healthy vegetation, but extreme values may indicate waterlogging. Water features were extracted using NDWI. Values from -1 to 0 correspond to drought and nonaqueous structures; pixels with values below 0.2 are humid or experience floods. All values above 0.2 correspond to surface water. However, it may vary due to the sediments present in the water. Dry, bare, and built areas are preferred in case of InSAR processing, as vegetation and water are sources of coherence loss. The quality index (Eq. 3.17) was calculated for both SAR tracks to compare the influence of the acquisition geometry (Fig. 13). Each pixel has a value in the range from -1 to 1, where positive values represent areas of high potential. The results are strongly dependent on the radar contributions. The dam is divided into two groups reflecting its sides. The highest quality is expected at the crowning, while the poorest results are expected to be observed on the water-facing side. This was confirmed in preliminary studies, since no persistent scatterers were found in that area, even considering its good backscattering properties.

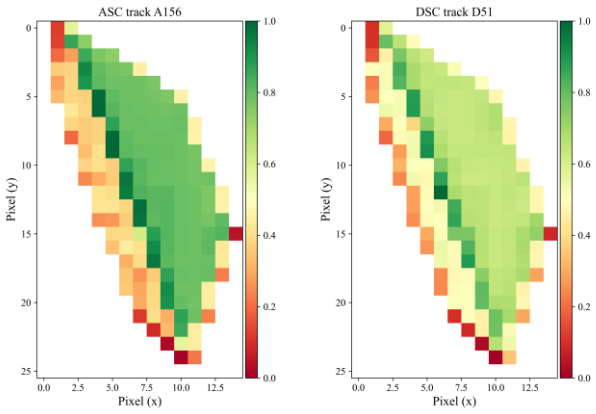

Fig. 13. Quality index for ascending (left) and descending (right) tracks – Nocelle dam

The radar contributions to the quality index are independent of time, as they represent a function of the relative geometry between the satellite and the surface of the AOI. On the contrary, multispectral contributions are time dependent as the indices are created based on the acquired soil conditions. Therefore, the quality index is not time invariant. However, if the AOI does not undergo major changes or environmental phenomena during the analysis period, the value of the Q_{index} is not expected to change significantly.

In order to ensure conciseness, the validation step is shown for just two pixels, representative for high and low quality, respectively (Fig. 14). The most relevant outcome that emerges is that when good quality is predicted by the Q_{Index}, the SAR coherence parameters of the linear regression are significantly different from zero (e.g., the H0 hypothesis of being statistically equal to zero is rejected). Conversely, when low quality is expected, the mean represents the best possible prediction, being little to no meaningful to the overall SMMI time series. The NRMSE value, instead, is more complicated to be interpreted as the SMMI values were normalized, and thus, the variability is limited to the range from 0 to 1. Larger values for pixels of poor quality are expected and obtained in most cases, but with discrepancies that can change based on the SMMI variability range of each pixel. As a consequence, we can state that the obtained results provide a successful validation of the proposed quality index.

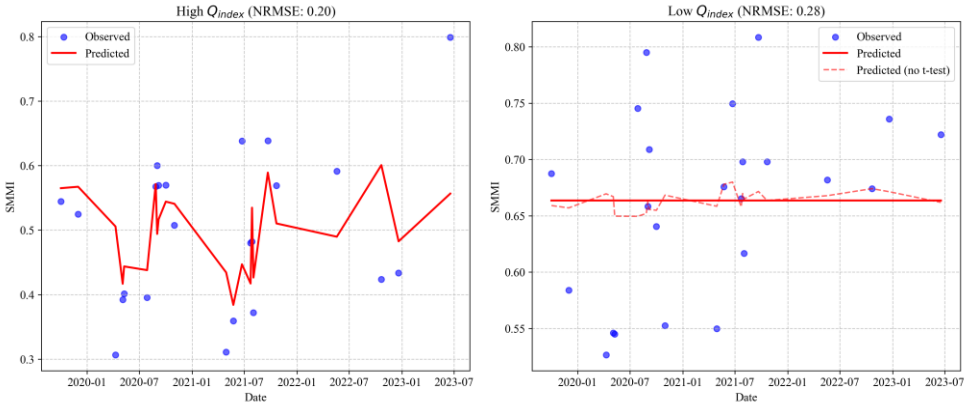

Fig. 14. Linear regression prediction of SMMI using SAR coherence data for a pixel showing high Q_{index} value and for one showing low Q_{index} value – Nocelle dam, track A146

5. DISCUSSION

The aim of the analysis was to explore the relationship between various products derived from radar and optical remote sensing satellites and to investigate their potential in monitoring soil moisture. Previous studies exploited mainly SAR backscatter intensity for this purpose. Radar images are combined with a single multispectral index such as NDVI [11, 18], NDMI [51] or NDWI [25]. This study analyzed more indices based on reflectance in various spectral bands to see whether some are more consistent with SAR coherence. The relationship between interferometric coherence and multispectral indices is intricate and linear regression models appear to be a suitable initial approach. However, more sophisticated relationship models, even machine learning (ML) algorithms, may be necessary to accurately model how alterations in environmental conditions impact both MS indices and SAR coherence. Soil moisture, as well as vegetation, undergo seasonal changes that can be observed in the temporal profiles of the selected MS indices. In the study [28], a strong relationship between SAR-derived soil moisture and annual precipitation records was discovered. The observed variations were following the seasonal patterns. Similar behavior is observed in temporal plots of correlation in both AOIs (Figs. 4, 5). Soil moisture changes not only throughout the season following its annual cycle [32], but also on a sub-daily basis [33]. Satellite images are acquired at the same time of day, thus computed indices shall be free from sub-daily variations. Several indices were used because the application of a single one is not robust and may lead to misinterpretation. For example, NDWI is insensitive to distinguish between water and built-up features [50]. Another factor that may have a significant impact on the quality of the analysis is the size of the AOI. The Italian and Polish sites differ in both extent and land cover homogeneity. The dam is more uniform in terms of land cover classes and within each of the classes. The vegetated area is mainly covered with grass. As it was presented in [10], the quality of soil moisture depends on the type of crops, showing that even variability within one land cover class can affect the final result in a significant way. In [51] soil moisture content was predicted considering various complexities of test areas, from grasslands, shrublands to entire landscapes. In Kosakowo, Poland, the AOI is composed of multiple structures, pavements, and fields, covering several square kilometers. However, the dam in Italy is a single structure, limited in size. Therefore, subdivision of the Polish AOI into smaller, more homogenous units could improve the correlation and help to identify areas of weaker and stronger correlation with interferometric coherence.

The temporal analysis of the correlation allowed us to identify two groups of indices. The vegetation-associated indices exhibit a negative linear relationship with the coherence level. This is because vegetation growth and probable movement of leaves and grass due to influence of wind, alter the scattering mechanism from one radar acquisition to the next. On the other hand, the water-related and built-up indices show a positive linear correlation with SAR coherence. These indices identify areas of the built environment that are more likely to maintain stability in backscattering. This is valid, as both AOIs do not include surface water reservoirs, which, instead, would have had a negative effect on the coherence level. Nevertheless, the temporal profiles of correlation are promising as analogous patterns (Fig. 6) can be spotted in both case study areas. The different magnitude of the correlation might be caused by the differences in the land cover and size of the two AOIs. As the Italian case site has a smaller spatial extent and is more uniform in land cover compared to the Polish AOI, it was selected for testing the proposed workflow.

6. CONCLUSION

In this study, an in-depth statistical analysis of the relationship between interferometric coherence and common multispectral indices for assessment of vegetation condition and surface water changes, with the purpose to analyze soil moisture, was conducted. The proposed quality index proved to be effective in pinpointing areas where radar coherence and spectral indices show a high correlation, enhancing the potential for targeted monitoring of hydrological and vegetation dynamics. While the findings provide a foundation, additional variables such as land surface temperature and precipitation, could be incorporated to refine the model, offering a deeper understanding of soil moisture variation across diverse environmental conditions. However, observed relationships are complex and linear regression may be insufficient to describe the dependencies between the analyzed components. More advanced machine learning models could be applied to further analyze the results obtained in this study.
Future research could explore predictive modeling, with the aim of estimating soil moisture from radar images, as they are independent of cloud cover. Furthermore, the integration of ground truth data and field samples would be essential to validate and refine these findings, paving the way for more accurate and reliable soil moisture estimation frameworks. This research provides a promising foundation, with considerable implications for advancing remote sensing in soil moisture and surface water dynamics monitoring studies.

ADDITIONAL INFORMATION

The work was supported by the project Minigrants for doctoral students of the Wrocław University of Science and Technology [50SD/0035/24]. The work was supported by the National Centre for Research and Development, Poland that financed the project “Closed-Loop Impact Monitoring for Environmentally and Socially Acceptable Energy Transition in Rural Regions”, acronym CLEAR [WPN/4/67/CLEAR/2022].

REFERENCES

1. Liu, G, Fu, H, Zhu, J, Wang, C and Xie, Q 2021. Penetration Depth Inversion in Hyperarid Desert From L-Band InSAR Data Based on a Coherence Scattering Model. *IEEE Geoscience and Remote Sensing Letters* **18**, 1981–1985.

2. Zhu, J, Liu, Z, Fu, H, Zhou, C, Zhou, Y, Wang, H and Xie, Y 2023. High-resolution sub-canopy topography mapping via TanDEM-X DEM combined with future P-band BIOMASS PolInSAR data. *Journal of Geod* **97**, 114.
3. Conversi, S, Carrion, D, Norcini, A and Riva, M 2023. Integrating Optical And Radar Imagery To Enhance River Drought Monitoring. The International Archives of the Photogrammetry, *Remote Sensing and Spatial Information Sciences* **XLVIII-1-W2-2023**, 1363–1371.
4. Chen, Z and Zhao, S 2022. Automatic monitoring of surface water dynamics using Sentinel-1 and Sentinel-2 data with Google Earth Engine. *International Journal of Applied Earth Observation and Geoinformation* **113**, 103010.
5. den Besten, N, Steele Dunne, S, Mahmud, A, Jackson, D, Aouizerats, B, de Jeu, R, Burger, R, Houborg, R, McGlinchey, M and van der Zaag, P 2023. Understanding Sentinel-1 backscatter response to sugarcane yield variability and waterlogging. *Remote Sensing of Environment* **290**, 113555.
6. Han, F, Zhang, X, Yu, J, Xu, S, Zhou, G and Li, S 2024. Study on spatiotemporal dynamic characteristics of precipitation and causes of waterlogging based on a data-driven framework. *Science of The Total Environment* **913**, 169796.
7. Nóia Júnior, R de S, Asseng, S, García-Vila, M, Liu, K, Stocca, V, dos Santos Vianna, M, Weber, TKD, Zhao, J, Palosuo, T and Harrison, MT 2023. A call to action for global research on the implications of waterlogging for wheat growth and yield. *Agricultural Water Management* **284**, 108334.
8. Lefebvre, G, Davranche, A, Willm, L, Campagna, J, Redmond, L, Merle, C, Guelmami, A and Poulin, B 2019. Introducing WIW for Detecting the Presence of Water in Wetlands with Landsat and Sentinel Satellites. *Remote Sensing* **11**, 2210.
9. Räsänen, A, Tolvanen, A and Kareksela, S 2022. Monitoring peatland water table depth with optical and radar satellite imagery. *International Journal of Applied Earth Observation and Geoinformation* **112**, 102866.
10. Bazzi, H, Baghdadi, N, Nino, P, Napoli, R, Najem, S, Zribi, M and Vaudour, E 2024. Retrieving Soil Moisture from Sentinel-1: Limitations over Certain Crops and Sensitivity to the First Soil Thin Layer. *Water* **16**, 40.
11. Montaldo, N, Fois, L and Corona, R 2021. Soil Moisture Estimates in a Grass Field Using Sentinel-1 Radar Data and an Assimilation Approach. *Remote Sensing* **13**, 3293.
12. Skulovich, O and Gentine, P 2023. A Long-term Consistent Artificial Intelligence and Remote Sensing-based Soil Moisture Dataset. *Scientific Data* **10**, 154.
13. van Hateren, TC, Chini, M, Matgen, P, Pulvirenti, L, Pierdicca, N and Teuling, AJ 2023. On the potential of Sentinel-1 for sub-field scale soil moisture monitoring. *International Journal of Applied Earth Observation and Geoinformation* **120**, 103342.
14. Yang, X, Chen, Y and Wang, J 2020a. Combined use of Sentinel-2 and Landsat 8 to monitor water surface area dynamics using Google Earth Engine. *Remote Sensing Letters* **11**, 687–696.
15. Yang, X, Qin, Q, Yésou, H, Ledauphin, T, Koehl, M, Grussenmeyer, P and Zhu, Z 2020b. Monthly estimation of the surface water extent in France at a 10-m resolution using Sentinel-2 data. *Remote Sensing of Environmen*t **244,** 111803.
16. Abd-Elaty, I, Kuriqi A, Pugliese, L, Zelenakova, M and El Shinawi, A 2023. Mitigation of urban waterlogging from flash floods hazards in vulnerable watersheds. *Journal of Hydrology: Regional Studies* **47**, 101429.
17. Bhogapurapu, N, Dey, S, Homayouni, S, Bhattacharya, A and Rao, YS 2022. Field-scale soil moisture estimation using sentinel-1 GRD SAR data. *Advances in Space Research* **70**, 3845–3858.

18. El Hajj, M, Baghdadi, N, Zribi, M and Bazzi, H 2017. Synergic Use of Sentinel-1 and Sentinel-2 Images for Operational Soil Moisture Mapping at High Spatial Resolution over Agricultural Areas. *Remote Sensing* **9**, 1292.
19. Sadeghi, M, Jones, SB and Philpot, WD 2015. A linear physically-based model for remote sensing of soil moisture using short wave infrared bands. *Remote Sensing of Environment* **164**, 66–76.
20. Singh, A, Gaurav, K, Sonkar, GK and Lee, CC 2023. Strategies to Measure Soil Moisture Using Traditional Methods, Automated Sensors, Remote Sensing, and Machine Learning Techniques: Review, Bibliometric Analysis, Applications, Research Findings, and Future Directions. *IEEE Access* **11**, 13605–13635.
21. Basargin, N, Alonso-González, A and Hajnsek, I 2024. *Comparison of Interferometric Soil Moisture Model and F-SAR Data Over Agricultural Areas at C- and L-Bands*. IGARSS 2024 - 2024 IEEE International Geoscience and Remote Sensing Symposium, Athens, Greece, 10715–10718.
22. Le, TS, Harper, R and Dell, B 2023. Application of Remote Sensing in Detecting and Monitoring Water Stress in Forests. *Remote Sensing* **15**, 3360.
23. Yi, Z, Liu, M, Liu, X, Wang, Y, Wu, L, Wang, Z and Zhu, L 2021. Long-term Landsat monitoring of mining subsidence based on spatiotemporal variations in soil moisture: A case study of Shanxi Province, China. *International Journal of Applied Earth Observation and Geoinformation* **102**, 102447.
24. Mao, K, Wang, H, Shi, J, Heggy, E, Wu, S, Bateni, SM and Du, G 2023. A General Paradigm for Retrieving Soil Moisture and Surface Temperature from Passive Microwave Remote Sensing Data Based on Artificial Intelligence. *Remote Sensing* **15**, 1793.
25. Alam, R, Quayyum, Z, Moulds, S, Radia, MA, Sara, HH, Hasan, MT and Butler, A 2023. Dhaka city water logging hazards: area identification and vulnerability assessment through GIS-remote sensing techniques. *Environmental Monitoring and Assessment* **195**, 543.
26. Sadeghi, M, Babaeian, E, Tuller, M and Jones, SB 2017. The optical trapezoid model: A novel approach to remote sensing of soil moisture applied to Sentinel-2 and Landsat-8 observations. *Remote Sensing of Environment* **198**, 52–68.
27. Sadeghi, M, Mohamadzadeh, N, Liang, L, Bandara, U, Caldas, MM and Hatch, T 2023. A new variant of the optical trapezoid model (OPTRAM) for remote sensing of soil moisture and water bodies. *Science of Remote Sensing* **8**, 100105.
28. Shen, Q, Wang, H, Shum, CK, Jiang, L, Yang, B, Zhang, C, Dong, J, Gao, F, Lai, W and Liu, T 2023. Soil Moisture Retrieval From Multipolarization SAR Data and Potential Hydrological Application. *IEEE Journal of Selected Topics in Applied Earth Observations and Remote Sensing* **16**, 6531–6544.
29. Normand, JCL and Heggy, E 2024. *Characterizing Surface Erosion and Soil Moisture Changes From Sparse Rainstorms in Karstic Deserts Using InSAR Coherence and Multi-Spectral Indices*. IGARSS 2024 - 2024 IEEE International Geoscience and Remote Sensing Symposium, Athens, Grece, 10076–10079.
30. Karamvasis, K and Karathanassi, V 2023. Soil moisture estimation from Sentinel-1 interferometric observations over arid regions. *Computers & Geosciences* **178**, 105410.
31. Baghdadi, N, Cerdan, O, Zribi, M, Auzet, V, Darboux, F, El Hajj, M and Kheir, RB 2008. Operational performance of current synthetic aperture radar sensors in mapping soil surface characteristics in agricultural environments: application to hydrological and erosion modelling. *Hydrological Processes* **22**, 9–20.
32. Hrysiewicz, A, Holohan, EP, Donohue, S and Cushnan, H 2023. SAR and InSAR data linked to soil moisture changes on a temperate raised peatland subjected to a wildfire. *Remote Sensing of Environment* **291**, 113516.

33. Villarroya-Carpio, A, Lopez-Sanchez, JM, Aguasca, A, Mas, M, Fàbregas, X, Broquetas, A and Steele-Dunne, SC 2024. Decorrelation rate and daily cycle in sub-daily time series of SAR coherence amplitude. *Remote Sensing of Environment* **313**, 114358.
34. Tarkowski, R, Lankof, L, Luboń, K and Michalski, J 2024. Hydrogen storage capacity of salt caverns and deep aquifers versus demand for hydrogen storage: A case study of Poland. *Applied Energy* **355**, 122268.
35. Torres, R, Snoeij, P, Geudtner, D, Bibby, D, Davidson, M, Attema, E, Potin, P, Rommen, B, Floury, N, Brown, M, Traver, IN, Deghaye, P, Duesmann, B, Rosich, B, Miranda, N, Bruno, C, L'Abbate, M, Croci, R, Pietropaolo, A, Huchler, M and Rostan, F 2012. GMES Sentinel-1 mission. *Remote Sensing of Environment* **120**, 9–24.
36. Gorelick, N, Hancher, M, Dixon, M, Ilyushchenko, S, Thau, D and Moore, R 2017. Google Earth Engine: Planetary-scale geospatial analysis for everyone. *Remote Sensing of Environment* **202**, 18–27.
37. Foumelis, M, Delgado Blasco, JM, Desnos, Y-L, Engdahl, M, Fernandez, D, Veci, L, Lu, J and Wong, C 2018. *Esa Snap - Stamps Integrated Processing for Sentinel-1 Persistent Scatterer Interferometry*. IGARSS 2018 - 2018 IEEE International Geoscience and Remote Sensing Symposium, Valencia, Spain, 1364–1367.
38. Monti, R and Rossi, L 2025. PHASE: a Matlab-based software for the DInSAR PS processing. *Geodesy and Cartography* **51**, 88–99.
39. Osmanoğlu, B, Sunar, F, Wdowinski, S and Cabral-Cano, E 2016. Time series analysis of InSAR data: Methods and trends. *ISPRS Journal of Photogrammetry and Remote Sensing* **115**, 90–102.
40. Ferretti, A, Monti-Guarnieri, A, Prati, C, Rocca, F and Massonet, D 2007. InSAR Principles - Guidelines for SAR Interferometry Processing and Interpretation (TM-19). *ESA Training Manual* 19.
41. Touzi, R, Lopes, A, Bruniquel, J and Vachon, PW 1999. Coherence estimation for SAR imagery. *IEEE Transactions on Geoscience and Remote Sensing* **37**, 135–149.
42. Zebker, HA, Hensley, S, Shanker, P and Wortham, C 2010. Geodetically Accurate InSAR Data Processor. *IEEE Transactions on Geoscience and Remote Sensing* **48**, 4309–4321.
43. Zupanc, A 2020. Improving Cloud Detection with Machine Learning. Sentinel Hub Blog. URL https://medium.com/sentinel-hub/improving-cloud-detection-with-machine-learning-c09dc5d7cf13 (accessed 10.10.24).
44. Feyisa, GL, Meilby, H, Fensholt, R and Proud, SR 2014. Automated Water Extraction Index: A new technique for surface water mapping using Landsat imagery. *Remote Sensing of Environment* **140**, 23–35.
45. McFeeters, SK 1996. The use of the Normalized Difference Water Index (NDWI) in the delineation of open water features. *International Journal of Remote Sensing* **17**, 1425–1432.
46. Xu, H 2006. Modification of normalised difference water index (NDWI) to enhance open water features in remotely sensed imagery. *International Journal of Remote Sensing* **27**, 3025–3033.
47. Gao, B 1996. NDWI—A normalized difference water index for remote sensing of vegetation liquid water from space. *Remote Sensing of Environment* **58**, 257–266.
48. Rouse, J, Haas, RH, Schell, JA and Deering, D 1973. Monitoring vegetation systems in the great plains with ERTS.
49. Zha, Y, Gao, J and Ni, S 2003. Use of normalized difference built-up index in automatically mapping urban areas from TM imagery. *International Journal of Remote Sensing* **24**, 583–594.
50. Ji, L, Zhang, L and Wylie, B 2009. Analysis of Dynamic Thresholds for the Normalized Difference Water Index. *Photogrammetric Engineering & Remote Sensing* **75**, 1307–1317.

51. Monteiro, AT, Arenas-Castro, S, Punalekar, SM, Cunha, M, Mendes, I, Giamberini, M, Marques da Costa, E, Fava, F and Lucas, R 2024. Remote sensing of vegetation and soil moisture content in Atlantic humid mountains with Sentinel-1 and 2 satellite sensor data. *Ecological Indicators* **163**, 112123.